surfaces

MDPI

Article

Exploring Bismuth Oxide Supported Kaolinite for Photocatalytic Application

Punyanuch Thammaacheep [1], Pornpraphatson Phetthai [1], Suthitra Suchai [1], Panatda Jannoey [2,3] and Duangdao Channei [1,3,4,*]

[1] Department of Chemistry, Faculty of Science, Naresuan University, Phitsanulok 65000, Thailand; punyanuchth66@nu.ac.th (P.T.)
[2] Department of Biochemistry, Faculty of Medical Science, Naresuan University, Phitsanulok 65000, Thailand; panatdaj@nu.ac.th
[3] Center of Excellence for Innovation and Technology for Detection and Advanced Materials, Faculty of Science, Naresuan University, Phitsanulok 65000, Thailand
[4] Centre of Excellence for Innovation and Technology for Water Treatment, Naresuan University, Phitsanulok 65000, Thailand
* Correspondence: duangdaoc@nu.ac.th; Tel.: +66-842426993

Abstract: Bismuth oxide (Bi_2O_3) and Bi_2O_3–supported Kaolin were synthesized using household microwave–assisted methods (350 W, 5 min), with catalyst characteristics analyzed. XRD patterns confirmed the monoclinic structure of Bi_2O_3. Incorporating 20%*w*/*w* Kaolin increased the specific surface area of Bi_2O_3 from 6.2879 to 16.1345 m^2/g, observed in FESEM images showing a hierarchical flower-like morphology resembling French fries alongside Kaolin plates. XRF analysis identified elements in Kaolin contributing to self–doping in band structure of Bi_2O_3, reducing its band gap and PL intensity. Kaolin/Bi_2O_3 composites demonstrated enhanced photocatalytic degradation of tetracycline (TC) under visible light, attributed to Bi_2O_3-generated radicals and increased surface area. The composite photocatalyst can be recycled up to three times. This research not only enhances the photocatalytic activity of Bi_2O_3 but also increases the value of a local waste material, Kaolin clay. Such enhancements could potentially extend to other metal oxides and abundant waste materials within the country.

Keywords: photocatalysis; bismuth oxide; tetracycline; kaolin

Citation: Thammaacheep, P.; Phetthai, P.; Suchai, S.; Jannoey, P.; Channei, D. Exploring Bismuth Oxide Supported Kaolinite for Photocatalytic Application. *Surfaces* **2024**, *7*, 698–713. https://doi.org/10.3390/surfaces7030045

Academic Editors: Gazi A. K. M. Rafiqul Bari, Zhong Chen and Md. Mahbubur Rahman

Received: 24 July 2024
Revised: 30 August 2024
Accepted: 1 September 2024
Published: 3 September 2024

1. Introduction

Semiconductor photocatalysts have gained significant interest for their potential applications in breaking down organic compounds. Among these, TiO_2 stands out as a widely utilized photocatalyst, known for its excellent chemical stability, potent oxidizing capability, and non-toxic nature [1,2]. However, its functionality is limited to ultraviolet light, which constitutes less than 5% of total sunlight, making it challenging for practical applications. As a result, many researchers have dedicated efforts to developing visible-light photocatalysts, among which are bismuth-containing semiconductors like BiOX (X = Cl, Br, I) [3–5], Bi_2WO_6 [6], Bi_2MoO_6 [7], $BiVO_4$ [8,9], and Bi_2O_3 [10–15].

The latter, bismuth oxide (Bi_2O_3), is gaining more attention due to its non-toxicity, stability in heat, eco-friendliness, high visible light absorption, and effectiveness in oxidation when used as a photocatalyst [16].

Bi_2O_3 typically exists in different phases and crystallite forms. The predominant phases include the alpha (α) phase, characterized by a monoclinic crystal structure, the beta (β) phase with a tetragonal crystal structure, and the gamma (γ) phase with a cubic crystal structure. Each phase has distinct crystal structures and properties [17,18]. Notably, the alpha (α) phase is the most stable at room temperature, and it has demonstrated

effectiveness in the photocatalytic degradation of certain harmful pollutants with a discrete band gap of ~2.2–2.8 eV [19].

On the part of synthesis, there are several methods for the synthesis of Bi_2O_3. Table 1 provides summarized data for the synthesis of Bi_2O_3, including the precursor, steps of synthesis, and disadvantages of conventional methods. Notable among these conventional methods are solid-state reaction, the hydrothermal method, sol–gel, co-precipitation, and ultrasound-assisted methods. Many of these approaches involve multiple processing steps and longer reaction times. Among the methods mentioned in Table 1, the microwave-assisted method is a simple and effective way of generating nanoparticles, offering several advantages compared to conventional methods. The key advantages of this method include two factors: (i) rapid reaction rates, as microwave irradiation enables the swift and uniform heating of the reaction mixture, leading to accelerated reaction rates, which can significantly reduce the synthesis time compared to traditional methods; and (ii) uniform heating: microwave irradiation ensures uniform heating throughout the reaction volume, promoting homogeneous nucleation and growth of nanoparticles. This can lead to more uniform and reproducible particle sizes [20,21]. To overcome the dependency on specialized microwave equipment, household microwave ovens were selected in this study, with control over wattage and time. The phase structures, morphologies, and optical absorption properties of the synthesized Bi_2O_3 were examined.

Table 1. Common synthesis methods of Bi_2O_3 powder.

Synthesis Method	Steps of Synthesis	Disadvantages	Ref.
Solid-State Reaction	Mixing of precursors, calcination at elevated temperatures followed by cooling and grinding.	Requires high temperatures and longer reaction times.	[10]
Hydrothermal Method	Aqueous reaction at high temperature and pressure.	High-pressure conditions and longer reaction times.	[11]
Sol–Gel Method	Solution preparation, gel formation through controlled hydrolysis, and heat treatment (drying and calcination).	Complex process and multiple processing steps.	[12]
Co-precipitation	Precipitation of bismuth hydroxide ($Bi(OH)_3$), washing, drying followed by calcination to produce Bi_2O_3.	Challenges in controlling particle size, agglomeration issues, and impurity incorporation.	[13]
Ultrasound-assisted method	Dissolving a bismuth precursor in a suitable solvent, applying ultrasound irradiation to induce formation and precipitation of Bi_2O_3 nanoparticles, followed by washing and drying.	High heat production during sonication, leading to the agglomeration of nanoparticles.	[14]
Microwave-assisted method	Preparing a precursor solution, subjecting to microwave irradiation for rapid heating, leading to the formation of Bi_2O_3 particles, followed by washing and drying.	Dependency on specialized microwave equipment and limited scalability for large-scale production.	[15]

Even though Bi_2O_3 is a widely used material with applications in various fields, one of its drawbacks is its low surface area, which can limit its effectiveness in certain applications. The surface area of a material is crucial in processes like catalysis, where more surface area provides more active sites for reactions to occur. Lately, there has been a growing interest in utilizing clays as carriers for metal oxide-based photocatalysts. These clays demonstrate the ability to adsorb organic substances both on their external surfaces and within their interlaminar spaces, attributed to their substantial surface area and significant pore volume. In addition, modified clay materials have found application in treating different pollutants. These modifications facilitate changes in the semiconductor structure, promoting enhanced

charge-separation mobility and, as a result, increasing the efficiency of photocatalytic oxidation processes [22,23].

Clay minerals, such as kaolinite, commonly known as kaolin, represent a type of clay mineral characterized by the chemical formula $Al_2Si_2O_5(OH)_4$. This mineral exhibits a layered silicate structure, linking a tetrahedral sheet of silica (SiO_4) linked to an octahedral sheet of alumina (AlO_6) through oxygen atoms. Kaolin holds significance as a crucial raw material in various industries and applications, including the production of high-quality ceramics, porcelain ceramics, paper, paints, and rubber, as well as in applications demanding chemical inertness and adsorption capabilities [24,25]. This material shows great potential for support because of its mechanical–chemical stability, cost-effectiveness, and effective adsorption capacity. These properties reduce the aggregation of metal oxide nanoparticles, resulting in improved photocatalytic performance.

Researchers have been developing mineral clay-modified photocatalysts from various types of mineral clay. For example, Oliveira et al. [26] employed titanium isopropoxide as a precursor to synthesize TiO_2 supported on fibrous clay (sepiolite). The immobilization of TiO_2 in the clay was achieved through the sol–gel method. The resulting samples exhibited a noteworthy 72% photocatalytic efficiency in discoloring eosin (EA) dye after 150 min under UV light. This high efficiency was attributed to the radicals produced by TiO_2 and the increased specific surface area modified by sepiolite. These findings suggest that TiO_2/sepiolite shows promise as a candidate for efficiently degrading organic pollutants. In relation to photocatalysis and the use of TiO_2, Zhang et al. [27] synthesized a new composite mixed-phase, TiO_2/kaolinite composites, and systematically studied the removal of acid red G (ARG) and 4–nitrophenol (4–NP), under UV light. According to the results, the enhanced photocatalytic performance of the TiO_2/Kaolin composite, which undergoes drying at 70 °C, can be attributed to various factors. These include the crystal structure and phase composition, effective charge separation, increased surface area, and higher adsorption capacity. In this same sense, Li et al. [28] synthesized TiO_2 nanoparticles assembled on kaolinites with varying morphologies, such as fake-like kaolinite (FK) and rod-like kaolinite (RK), using a simple precipitation method. They explored the effects of different operational parameters on the photocatalytic performance. The degradation of the antibiotics (tetracycline hydrochloride) was evaluated under UV light irradiation using TiO_2 and TiO_2/fake-like kaolinite composites. Overall, composites of TiO_2 with fake-like kaolinite exhibited superior stability and enhanced photocatalytic performance compared to alternative materials. This improvement is attributed to the synergistic influence of the two-dimensional morphology and enhanced adsorption capacity.

In this study, combining Bi_2O_3 with these porous materials can significantly increase the overall surface area of the composite material. This is advantageous in applications where a higher surface area is required for enhanced reactivity or adsorption. Additionally, the porous nature of clay or kaolinite introduces additional pore spaces in the composite material. These pores can act as reservoirs for molecules or facilitate the diffusion of reactants and products, improving the efficiency of certain processes. Moreover, clay minerals are abundant and relatively low-cost materials. Incorporating them into Bi_2O_3 can make the composite more cost-effective compared to using Bi_2O_3 alone, especially in large-scale applications. The mixed-phase Bi_2O_3 supported on kaolinite (Bi_2O_3/Kaolin) was synthesized by introducing the Bi cations precursor into the kaolinite medium by domestic microwave-assisted methods. The main objectives are to study the impact of kaolin on the structural, morphological, surface, and optical properties of Bi_2O_3.

While tetracycline, commonly used to treat bacterial infections, can be effective in combating such infections [29,30], its use and release into the environment can lead to harmful effects. Therefore, this study aimed to investigate the photocatalytic degradation of tetracycline under visible light exposure. The photocatalytic properties, as well as the adsorption activity of the Bi_2O_3/Kaolin composites, were evaluated in comparison to the single-phase Bi_2O_3.

2. Materials and Methods

The Kaolin powder (Kaolinite, $Al_2Si_2O_5(OH)_4$) found in Kaolin clay, obtained from Lampang, a province in northern Thailand, is an important source of raw material for ceramics. Bismuth(III) nitrate pentahydrate ($Bi(NO_3)_3{\cdot}5H_2O$, 98%) was supplied from KemAus™ (Cherrybrook, Australia). Tetracycline hydrochloride ($C_{22}H_{24}N_2O_8{\cdot}HCl \geq 95\%$) powder was obtained from Sigma-Aldrich (St. Louis, MO, USA). Sodium hydroxide (NaOH) Pellets and Nitric acid (HNO_3), Grade AR were supplied from the Merck Chemical Company (Rahway, NJ, USA). The materials were used as received without purification.

2.1. Synthesis of Bi_2O_3 Powders by Microwave-Assisted Method

The solutions, including 0.01 mol $Bi(NO_3)_3{\cdot}5H_2O$ in 50 mL of 1 mol/L HNO_3, were prepared at room temperature and were stirred for 10 min. The obtained solutions were mixed with 50 mL of 1.5 mol/L NaOH (dropwise) and stirred continuously for a period of 60 min until a precipitate was formed. The obtained mixture was introduced into a household microwave reactor and subjected to optimal conditions, with a power setting of 350 W for a duration of 5 min. During this period, we continuously released internal heat every minute and maintained this process for a total of 5 min to prevent the risk of suspension explosion. Finally, the Bi_2O_3 products were separated from the solvent by centrifugation, washed multiple times with distilled water, and dried in an oven at 100 °C for 120 min to eliminate any residual water content. The chemical reactions of each step and the chemicals used are shown as follows:

$$2Bi(NO_3)_3\ (aq) + 6NaOH\ (aq) \rightarrow Bi_2O_3\ (s) + 6NaOH\ (aq) + 3H_2O\ (l)$$

2.2. Synthesis of Bi_2O_3/Kaolin Composite by Microwave-Assisted Method

The Kaolin powder was ground, dried at 100 °C for 120 min, and then sieved to separate dense particles from the fine ones. Then, Kaolin powder was added in amounts of 20%w/w during the precursor-solution preparation step, and the heat treatment step followed the same procedure as that with Bi_2O_3.

2.3. Characterization

Elemental analysis was performed using a wavelength dispersive X-ray fluorescence (WDXRF) spectrometer (Rigaku, ZSX Primus, Auburn Hills, MI, USA). The samples were characterized using various analytical techniques. Powder X-ray diffraction (XRD) analysis was conducted with CuKα radiation on a Bruker Model: D2 PHASER instrument (Billerica, MA, USA) to determine their crystalline structure and phase composition. Surface area, pore volume, and pore size were analyzed using N_2 adsorption/desorption isotherms based on the Brunauer–Emmett–Teller (BET) theory, employing a Micromeritics Model: TriStar II 3020 instrument (Norcross, GA, USA). The morphology of the specimens was investigated using field-emission transmission electron microscopy (FESEM) with the Thermo Scientific Apreo model. Optical absorption spectra in the solid state were studied using UV–VIS diffuse reflectance spectroscopy (DRS UV–vis) with a Shimadzu UV-3101PC instrument (Kyoto, Japan). Photoluminescence spectra (PL) were recorded at room temperature with a Fluoromax-4 Horiba Jobin Yvon instrument (Kyoto, Japan), exciting at a wavelength of 350 nm. This instrument was also utilized to measure terephthalic acid (TA) formed with hydroxyl radicals, employing an excitation wavelength of 312 nm and a slit width of 5 nm at room temperature. The Nyquist plots were recorded using an Autolab PGSTAT302N (Herisau, Switzerland) at pH 6 with a Na_2SO_4 electrolyte (0.1 M) within a frequency range of 1–1000 Hz at an amplitude of 0.1.

2.4. Photocatalytic Activity Measurement

The effectiveness of Bi_2O_3 in comparison to Bi_2O_3-supported Kaolin for the photocatalytic degradation of TC was assessed in an aqueous environment. To conduct the experiment, the photocatalysis procedure was evaluated under controlled reaction condi-

tions: a photocatalyst dose of 0.05xx g and a TC concentration of 5 ppm (or mg/L) in a 100 mL reaction medium with a pH of 4.0.

Before light activation, dark adsorption experiments on Bi_2O_3/KO were conducted for 20, 30, 40, and 60 min to ensure adsorption/desorption equilibrium was achieved. Following this, the mixed suspension was kept in the dark for 30 min to maintain the conditions established during the dark adsorption experiments. The suspension was then exposed to visible light for 90 min using a 54 W halogen lamp with an intensity of 3.98 W/m^2, positioned approximately 30 cm from the suspension. The temperature of the photoreactor during the reaction was controlled at a constant 35.0 °C (or not exceeding 35.0 °C), using an industrial fan built into the chamber.

Photodegradation experiments were conducted in a batch photoreactor, as shown in Figure 1. It is important to note that each time interval was tested with a separate beaker to control the amount of catalyst and TC solution. If the suspension were to be taken from the same beaker, the ratio of solid catalyst to the concentration of the TC solution would change, and the temperature of the reduced suspension volume might increase during the final stage.

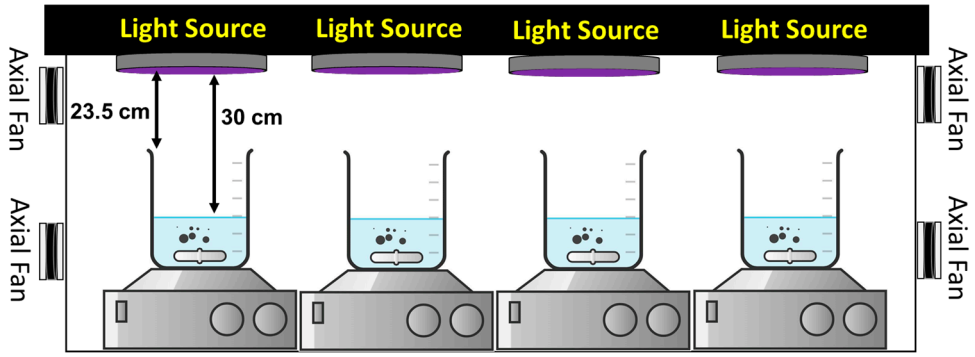

Figure 1. Schematic diagram of the photoreactor: 0.05 g photocatalyst mixed with 100 mL of 5 ppm TC, at pH = 4.5.

Throughout the interaction period, samples of 3.0 mL each were extracted at specified intervals and subsequently subjected to centrifugation at 5000 rpm for 10 min. The resulting supernatants were then analyzed using a MAPADA UV–6100 double-beam spectrophotometer (Shanghai, China) to measure the absorbance of TC at a wavelength of 350 nm. The changes in TC concentrations over time were determined by converting absorbance intensity using a calibration curve based on the Beer–Lambert law [31]. The percent degradation of the TC was calculated using Equation (1):

$$Degradation\ (\%) = 100 \times \left(\frac{C_0 - C_t}{C_0} \right) \quad (1)$$

Here, "C_0" represents the initial concentration of TC (mg/L), while "C_t" indicates the concentration of TC remaining (mg/L) at a specific time (t).

Additionally, a kinetic study was conducted to compare the reaction rates (k_1, min^{-1}) of each catalyst at the same temperature. The equation represented by Equation (2) below, is referred to as the pseudo-first-order model [32].

$$-\ln \frac{C_t}{C_0} = k_1 t \quad (2)$$

2.5. Detection of Hydroxyl Radical (•OH)

Hydroxyl radical-detection experiments were conducted using terephthalic acid (TA) as a probe molecule to detect hydroxyl radicals (•OH), as reported in many studies [33–35]. A 1000 mL aqueous solution of TA (0.08xx g, 5 × 10^{-4} M) was prepared and mixed

with 0.05xx g of Bi_2O_3 photocatalyst. The pH of the solution was adjusted to 8.0 using NaOH solution, by adding 0.24xx g to the 1000 mL solution to achieve a concentration of 6×10^{-3} M. The mixture was stirred for 30 min and then irradiated with a visible light lamp. Samples were taken at different time intervals (30, 60, and 90 min), and centrifuged to separate the composite. Finally, the fluorescence of the supernatant was measured by excitation at 312 nm.

3. Results

3.1. Microstructure Analysis

The Kaolin sample collected in this study was analyzed using an XRF instrument, and the results are presented in Table 2. The analysis identified that the Kaolin primarily contains SiO_2 and Al_2O_3, with compositions of approximately 49.6% and 48.8%, respectively, which is consistent with the typical composition of Kaolin (silicate and alumina). However, the sample also contains various impurities, including TiO_2, Fe_2O_3, P_2O_5, MgO, CaO, and other compounds.

Table 2. Sample chemical composition (%wt) in Kaolin.

Component	Unit (%wt)
SiO_2	49.6
Al_2O_3	48.8
TiO_2	0.53
Fe_2O_3	0.46
P_2O_5	0.22
MgO	0.18
CaO	0.06
Other compounds	0.15

The Kaolin structure was investigated by powder XRD, as shown in Figure 2a. The untreated Kaolin showed a diffraction pattern corresponding to crystalline-layered Kaolinite, consistent with JCPDS standards No. 00−900−9230 [36,37]. In Figure 2b, all diffraction peaks in the XRD pattern of the powder sample strongly correspond to the monoclinic α-Bi_2O_3 lattice planes. The observed XRD results match well with previously reported literature and JCPDS card no. 41–1449, which is consistent with the reports by H. Cheng et al. [38] and J. Eberl et al. [39].

Additionally, peaks corresponding to secondary crystalline phases of β-Bi_2O_3 (JCPDS No. 27–0050) were detected at 2θ values of 29.2°, 30.5°, and 31.5°, indicating the presence of a mixed phase. However, the primary phase remains α-Bi_2O_3. The distinct diffraction peaks of α-Bi_2O_3 demonstrates its high crystallinity. Conversely, in Figure 2c, β-Bi_2O_3/Kaolin exhibits broader and weaker diffraction peaks, indicating reduced crystallinity. No apparent peak of Kaolin was observed, which suggests that the Kaolin may be in an amorphous form or have low crystallinity.

The adsorption capabilities of the samples were studied using N_2 adsorption–desorption measurements. N_2 adsorption–desorption isotherms for the pure Bi_2O_3, Kaolin, and Bi_2O_3-supported Kaolin samples are depicted in Figure 3a–c, with corresponding BET equation results detailed in Table 3. According to the findings, the Bi_2O_3/Kaolin composite exhibits a larger specific surface area compared to pure Bi_2O_3. The BET surface area of Bi_2O_3, Kaolin, and Bi_2O_3/Kaolin was measured at 6.2879, 9.0365, and 16.1345 m^2/g, respectively. This increase may be attributed to the addition of Kaolin to Bi_2O_3, which results in a rougher surface, as depicted in the FESEM images.

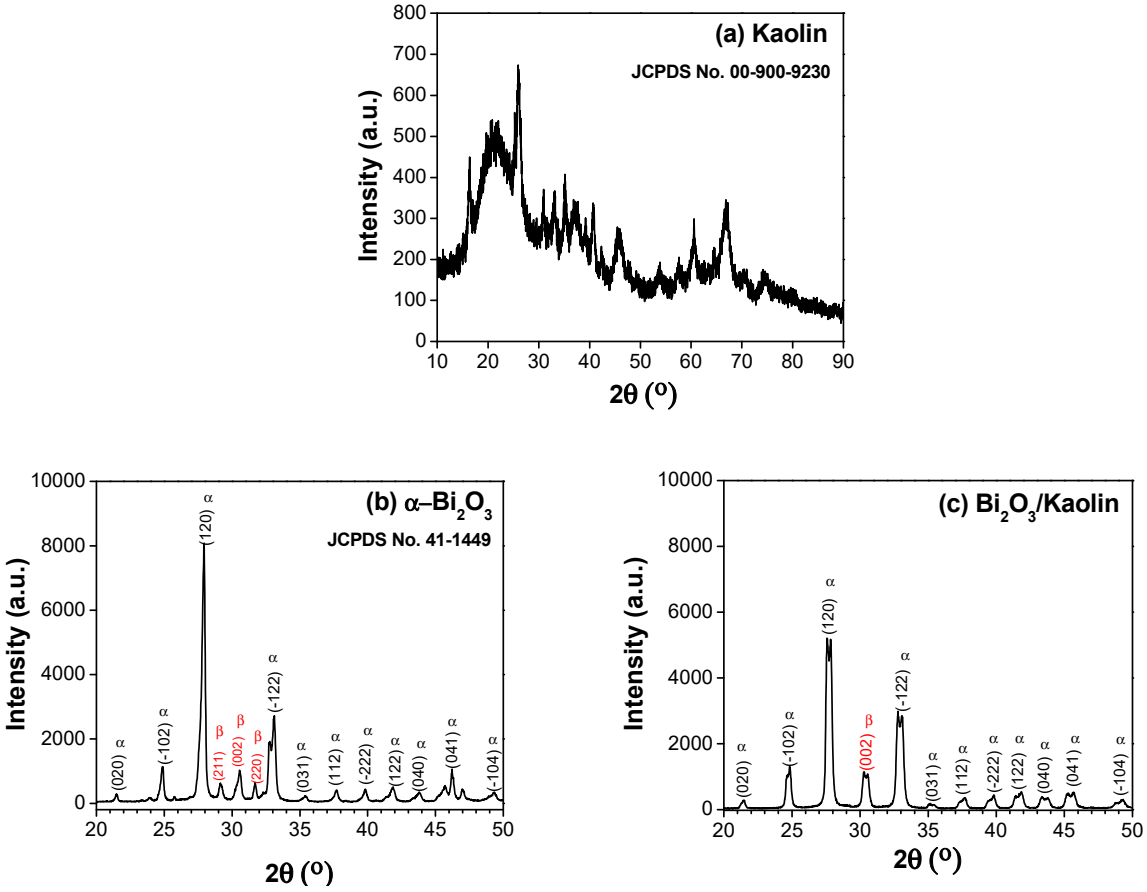

Figure 2. Powder XRD diffractogram of (**a**) pure Kaolin, (**b**) Bi_2O_3, and (**c**) Bi_2O_3/Kaolin composite.

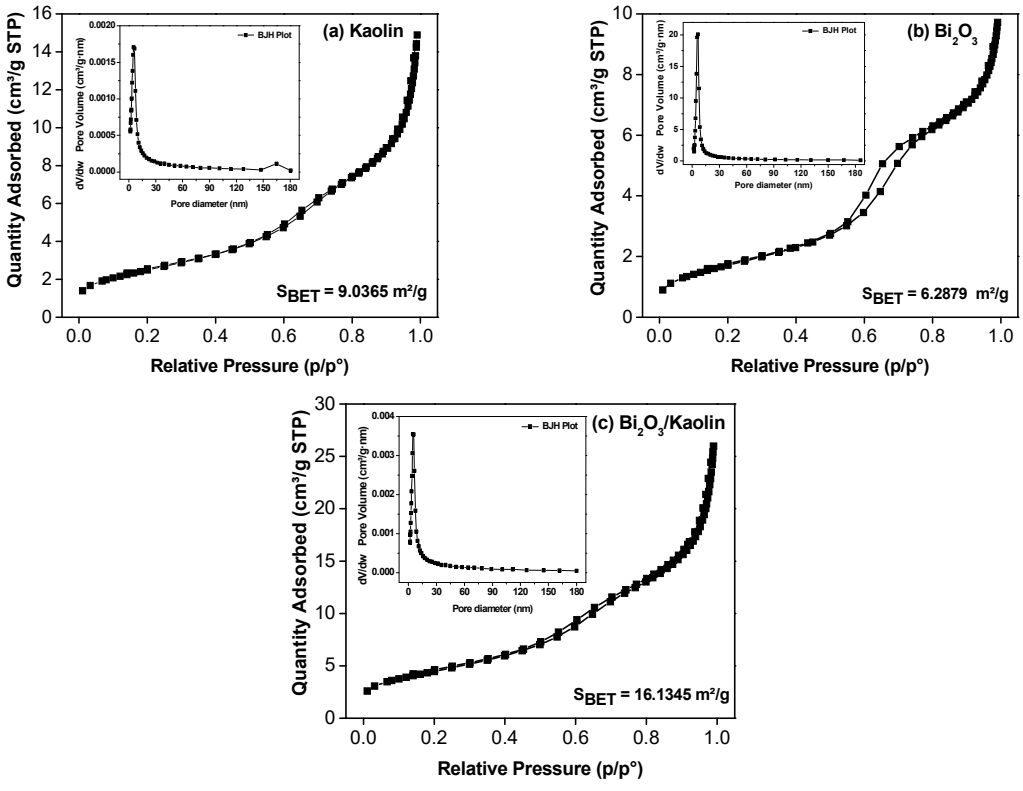

Figure 3. N_2 adsorption–desorption isotherms of (**a**) Kaolin, (**b**) Bi_2O_3, and (**c**) Bi_2O_3/Kaolin.

Table 3. Comparison of specific surface area of various prepared samples.

Samples	BET Surface Area (S_{BET}, m^2/g)	BJH Pore Size (nm)	Total Pore Volume (cm^3/g)
Bi_2O_3	6.2879	8.2698	0.01099
Kaolin	9.0365	9.6641	0.01382
Bi_2O_3-supported Kaolin	16.1345	9.3547	0.02454

The increase in the specific surface area of the Bi_2O_3/Kaolin composite enhances the feasibility of enhancing surface-active sites and facilitates charge transport. This structural modification accelerates the degradation of TC molecules during the photocatalytic process, thereby resulting in superior photocatalytic performance of the Bi_2O_3/Kaolin composite. According to the IUPAC classification, all adsorption–desorption isotherms exhibited type-IV curves accompanied by hysteresis loops, indicating the presence of mesoporous structures ranging in diameter from 2 to 50 nm. Additionally, the inset in Figure 3 illustrates the corresponding pore size distribution plots, measured from the adsorption isotherms of nitrogen isotherms using the Barrett–Joyner–Halenda (BJH) method. The mean pore diameters for Bi_2O_3, Kaolin, and the Bi_2O_3/Kaolin composite were 8.2698 nm, 9.6641 nm, and 9.3547 nm, respectively, all within the mesoporous range.

FESEM was employed to analyze the morphologies of the Bi_2O_3 obtained after the addition of Kaolin. The morphology and surface microstructure of all samples were initially magnified for comparison. The morphology of Kaolin depicted in Figure 4a,b appears predominantly as plates and large aggregations, with an average size of around 1 µm. The FESEM images in Figure 4c,d reveal that Bi_2O_3 exhibits an almost identical French-fries-like shape. The lengths of the Bi_2O_3 particles ranged from 1.0 to 5.3 µm, while their widths varied from 0.5 to 1.2 µm. As shown in Figure 4e,f, micromorphology of the Bi_2O_3/Kaolin composite displays a hierarchical flower structure formed by the assembly of Bi_2O_3 in a French-fries-like shape. Kaolin is present in the composite structure, with small particles identifiable on the surface of Bi_2O_3. The rough surface and complex morphology of the composite sample result in a higher surface area, enabling it to adsorb more TC molecules.

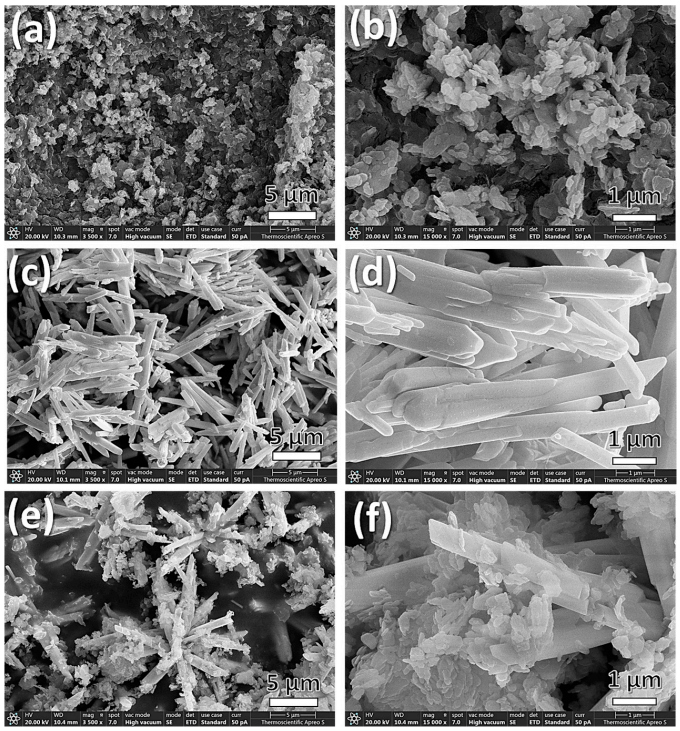

Figure 4. FESEM images of (**a**,**b**) Kaolin, (**c**,**d**) Bi_2O_3, and (**e**,**f**) Bi_2O_3-supported Kaolin at magnifications of 3500× and 15,000×.

The diffuse reflectance spectra of pure and Kaolin-doped Bi_2O_3 are shown in Figure 5a. The absorption spectra of the powder samples were acquired using the Kubelka–Munk method in DRS mode.

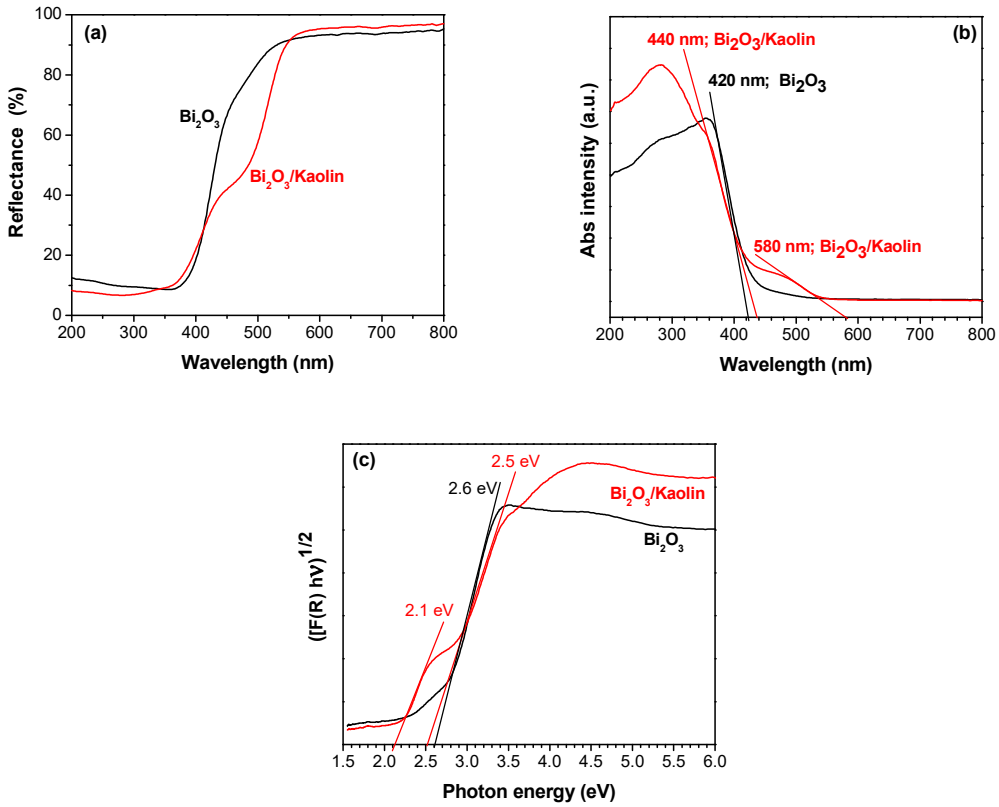

Figure 5. (**a**) Diffuse reflectance, (**b**) Kubelka–Munk curves and (**c**) band gap determination.

The Kubelka–Munk equation is expressed as $F(R) = (1 - R)^2/2R$, where R represents the reflectance and F(R) denotes the absorbance [40]. The F(R) curves of the samples, or absorbance spectra, are shown in Figure 5b. In pure Bi_2O_3 samples, there is an absorption peak at 420 nm, which represents the peak absorption wavelength where electrons are excited from the valence band to the conduction band. Kaolin-doped samples show a shift in the absorption peak to higher wavelengths in the visible region, with one peak occurring at 440 nm and another absorption hump appearing around 580 nm. The two-step change observed in the absorption spectra after doping might be due to the introduction of new energy levels within the band gap and alterations in the electronic structure of the Bi_2O_3. The doping with Kaolin could create defect states or impurity levels that facilitate additional electronic transitions, leading to the observed shifts in the absorption peaks. From the absorption spectra analysis of the samples, it is evident that doping Bi_2O_3 with Kaolin shifts its absorption edge. Consequently, the effective reduction in the band gap (E_g) of Bi_2O_3 can be determined, due to the incorporation of impurity ions from Kaolin. Figure 5c illustrates the comparison between the band gap of pure Bi_2O_3 and Kaolin-doped Bi_2O_3. For band gap determination, $[F(R)h\nu]^n$ is plotted against hν. Since monoclinic Bi_2O_3 is an indirect band-gap semiconductor, the value of = ½ (n = 2 for a direct band gap) [41]. The band gap is found by drawing a line on the linear part of the $[F(R)h\nu]^{(1/2)}$-versus-hν curve and identifying the intercept where $[F(R)h\nu]^{(1/2)}$ equals zero. The energy levels of Kaolin-doped Bi_2O_3 were found to be 2.1 eV and 2.5 eV, whereas the energy gap of pure Bi_2O_3 is 2.6 eV. Thus, with a decrease in the band gap, the energy associated with defects also increases.

This provides evidence that the formation of sub-band states between the valence and conduction bands results in the reduction of the band gap, depicted in the energy-level

diagram shown in Figure 6a. As shown in the proposed diagram, the valence band (VB) and conduction band (CB) could be determined using the following equations [42]:

$$E_{VB} = \chi - E_O + 0.5E_g \quad (3)$$

$$E_{CB} = E_{VB} - E_g \quad (4)$$

where E_O is the energy of free electrons in the hydrogen size (4.5 eV), χ is the absolute electronegativity of Bi_2O_3 (5.986 eV) [43], E_g is the calculated band gap of Bi_2O_3 (2.6 eV), and E_{VB} and E_{CB} are the valence-band edge and conduction-band edge, respectively.

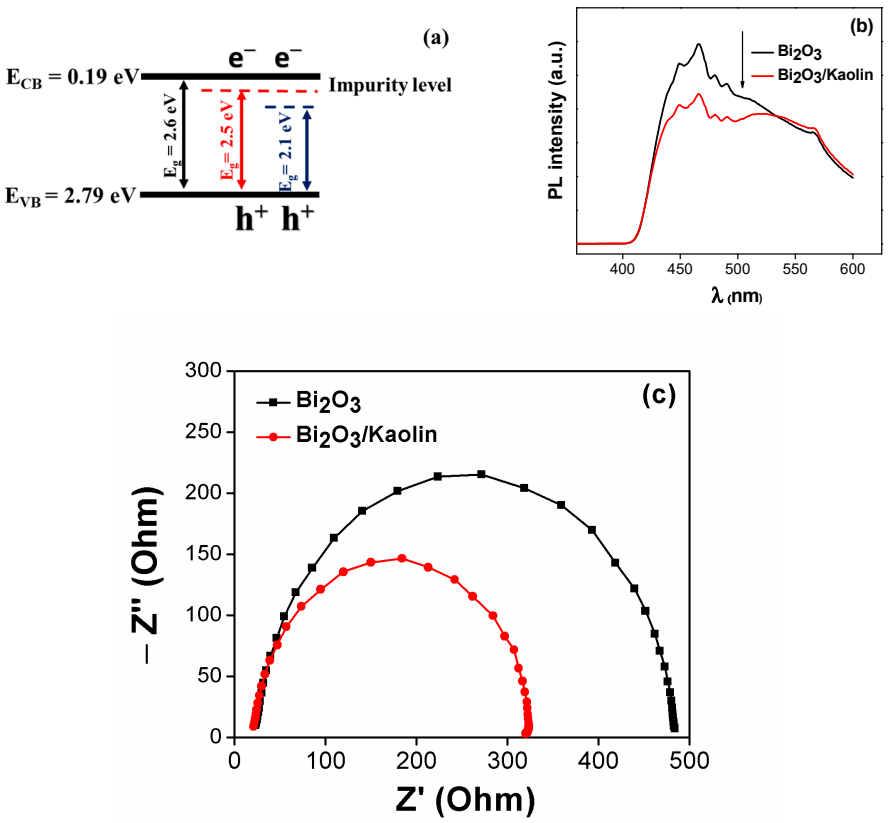

Figure 6. (**a**) Energy level diagram, (**b**) PL intensity, and (**c**) Nyquist plots of pure and Kaolin-doped Bi_2O_3.

Combined with the results with equations, the CB and VB values for the pure Bi_2O_3 are 0.19 eV and 2.79 eV, respectively.

Introducing impurities not only creates additional energy levels within the bandgap of the semiconductor but also acts as traps for electrons, resulting in a reduced recombination process, as shown in Figure 6b. Since photoluminescence (PL) intensity measures electron–hole recombination in semiconductors, higher intensity indicates increased electron recombination and photoluminescence signal release. Kaolin introduces defects or trap states, reducing electron–hole recombination and PL intensity. This suggests improved carrier separation and potentially enhanced charge transport in doped Bi_2O_3. This effect is also demonstrated in the research by L.T.S Thao et al. [44], where vetiver grass was added to a TiO_2 photocatalyst. The addition of rice straw not only reduced the bandgap energy but also provided impurities that helped trap electrons, leading to improved dye degradation. The Nyquist plot in the high-frequency region corresponds to the charge transfer resistance, while the smaller semicircle implies a reduced charge transfer resistance at the interfaces. Figure 6c shows that the radius of the Bi_2O_3/Kaolin composite (319.98 Ω) is smaller than that of pristine Bi_2O_3 (483.82 Ω), indicating that the introduction of Kaolin can reduce

the interfacial charge transfer resistance and improve the separation of photo-generated electron–hole pairs, consistent with the results from PL intensity.

3.2. Photocatalytic Performance

The photocatalytic activity of all prepared photocatalysts was evaluated by testing their degradation of TC under visible light irradiation for 90 min. This procedure was repeated twice, with a standard deviation of 5–7. Before the light was turned on, a suspension of the solid catalyst (0.05 g) in a 5 ppm TC solution was kept in the dark for 60 min to ensure that the observed degradation efficiency after light irradiation was not influenced by adsorption. As illustrated in Figure 7a, equilibrium was achieved at 30 min with an adsorption rate of 13.0% using the Bi_2O_3/KO composite. Therefore, a 30 min period was set for dark adsorption for the remaining samples.

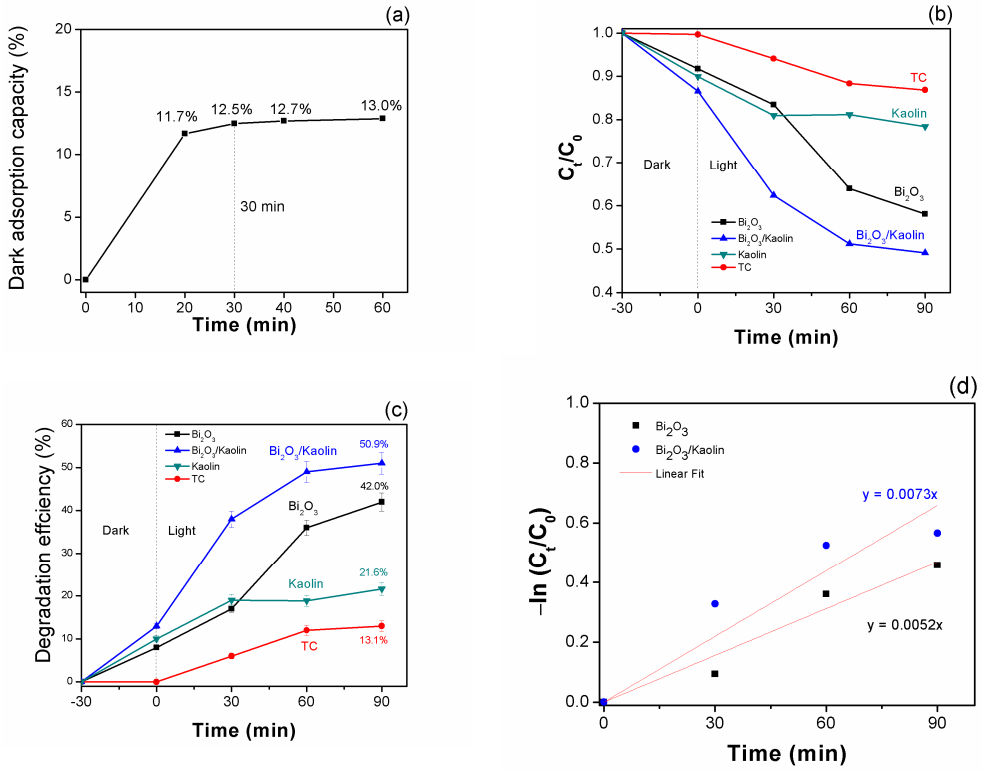

Figure 7. (**a**) Dark adsorption capacity, indicated by the dotted line, of Bi_2O_3/KO, (**b**) plot of C_t/C_o, (**c**) degradation efficiency, and (**d**) kinetic process of TC degradation vs. irradiation time: 0.05 g photocatalyst mixed with 100 mL of 5 ppm TC, at pH = 4.5.

As shown in Figure 7b,c, the adsorption in the dark for Kaolin, Bi_2O_3, and Kaolin–doped Bi_2O_3 were 10%, 8.3%, and 13.5%, respectively, ensuring that any degradation of TC after exposure to light is solely due to the photocatalytic response. Therefore, a higher BET surface area leads to greater degradation efficiency, as it enhances the adsorption of TC molecules on the catalyst surface, preparing them for the subsequent photocatalytic step.

After an additional 90 min of visible light exposure, the Bi_2O_3/Kaolin composite demonstrated the highest degradation efficiency at 50.9%, compared to pure Bi_2O_3, which achieved about 42.0%. Thus, adding Kaolin to Bi_2O_3 in the composite sample significantly impacts the absorption and degradation of TC. The difference between adsorption in the dark and efficiency under light represents the actual photocatalytic degradation efficiency. It was found that the photoactive efficiency of pure Bi_2O_3 was 33.7%, while the composite showed a slightly higher efficiency, at 37.4%. For Kaolin, the degradation efficiency remains constant at about 18 to 21.6%, whether in the dark or under light. Regarding the photolysis of TC, self-degradation reaches 13% by the end of the testing process. Figure 7d shows that

the Kaolin-doped Bi_2O_3 catalyst exhibits the highest photocatalytic degradation rate for TC (0.0073 min^{-1}), which is 1.4 times greater than that of pure Bi_2O_3 (0.0052 min^{-1}).

The reusability of the catalyst is a critical factor for industrial applications. Therefore, the recyclable performance of the Bi_2O_3/KO composites, which exhibited the highest efficiency, was tested under identical conditions. After the first run, centrifugation was employed to separate the solid catalyst from the TC liquid phase. The collected catalyst was then reused in subsequent runs. As illustrated in Figure 8a, the degradation efficiency of TC decreased from 50.9% to 32.3% and further declined to 25.5% after three recycling cycles. Additionally, there is an 18.6% difference between Cycle 1 and Cycle 2, and a 25.4% difference between Cycle 1 and Cycle 3. In many cases, Bi_2O_3-based photocatalysts can sustain their efficiency with a reduction of less than 20% over multiple cycles [45–47].

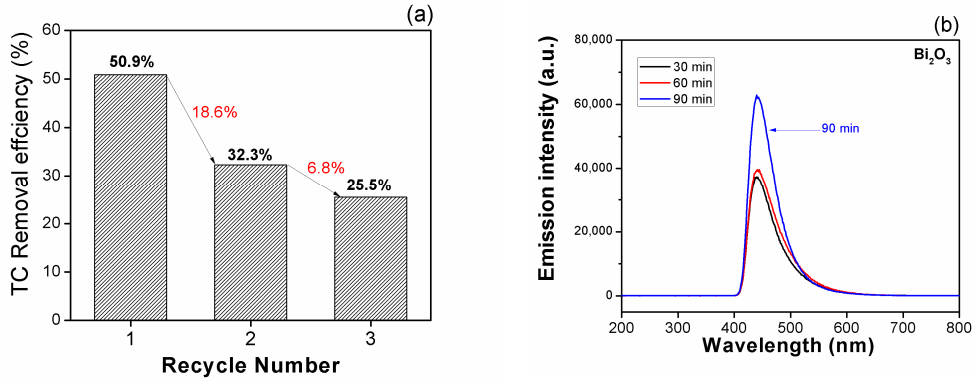

Figure 8. (**a**) Recovery and reuse of Bi_2O_3/KO composite and (**b**) change in fluorescence intensity observed during the irradiation of a 0.05xx g catalyst suspended in a 5×10^{-4} M TA solution and NaOH 6×10^{-3} M.

Thus, the use of two cycles of reuse in this study is acceptable, while continuing to a third cycle results in reduced efficiency. This may be attributed to changes in the surface morphology of the photocatalyst due to repeated cycles, which can lead to a reduction in surface area or alterations in the distribution of active sites.

The confirmation of hydroxy radical (•OH) formation by the Bi_2O_3 photocatalyst is represented in Figure 8b. In typical experiments, the intensity of fluorescence is directly related to the concentration of •OH radicals present in the system. The higher the concentration of hydroxyl radicals, the greater the fluorescence intensity observed. This observation indicates the generation of •OH radicals under light irradiation, which is consistent with the results of degradation experiments showing that the degradation effectiveness (%) increases with the increase in •OH formation.

Due to the confirmation of the existence of hydroxyl radicals (•OH), the photocatalytic mechanism, as shown in Figure 9, can be proposed and explained through the following steps.

(i) *Light absorption:* the process initiates when the Bi_2O_3 photocatalyst absorbs photons from incident light.

(ii) *Generation of electron–hole pairs:* when exposed to light, electrons within the valence band of the Bi_2O_3 photocatalyst become energized to the conduction band, creating positively charged holes (known as electron–hole pairs), in the process.

$$Bi_2O_3/Kaolin + h\nu \rightarrow e^- + h^+ \quad (5)$$

(iii) *Redox reactions:* the electrons in the conduction band and the holes in the valence band are both highly reactive species. They can participate in redox (reduction–oxidation) reactions with other molecules adsorbed onto the surface of the photocatalyst. The electron–hole pairs generated on the surface of the photocatalyst can react with O_2

molecules adsorbed from the surrounding environment, producing reactive oxygen species (ROS) such as superoxide radicals ($O_2\bullet^-$) and hydroxyl radicals (•OH).

$$e^- + O_2 \rightarrow \bullet O_2^- \quad (6)$$

$$2e^- + O_2 + 2H^+ \rightarrow H_2O_2 \quad (7)$$

$$H_2O_2 + \bullet O_2^- \rightarrow \bullet OH + OH^- \quad (8)$$

$$h^+ + H_2O \rightarrow \bullet OH + H^+ \quad (9)$$

(iv) *Adsorption of contaminants*: organic contaminants, such as the target molecule TC in this study, adsorb onto the surface of the Bi_2O_3 photocatalyst with the assistance of Kaolin.

(v) *Degradation of contaminants*: the generated ROS, particularly hydroxyl radicals, are highly oxidative and can react with the adsorbed organic contaminants, including TC, breaking down their molecular structure into smaller, less harmful molecules such as carbon dioxide, water, and other byproducts.

$$OH/O_2^- + TC \rightarrow CO_2 + H_2O \quad (10)$$

By following these steps, the combined Bi_2O_3/Kaolin photocatalyst effectively degrades organic contaminants like TC under irradiation, offering a promising solution for water purification and environmental remediation applications.

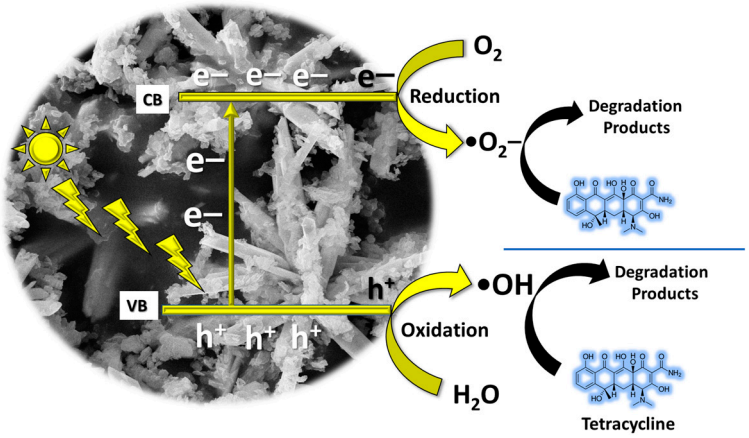

Figure 9. The photocatalytic mechanism of Kaolin-doped Bi_2O_3.

4. Conclusions

This study successfully synthesized Bi_2O_3 using a household microwave reactor in a rapid, single-step process that took only 5 min at a power of 350 W, and further modified it by incorporating Kaolin as a composite material.

- The addition of Kaolin to Bi_2O_3 did not alter its monoclinic crystal structure; however, it significantly reduced the band gap and created sub-band states that acted as non–radiative recombination centers.
- The addition of kaolin significantly increased the surface area of Bi_2O_3, enhancing its photocatalytic degradation efficiency, which is the primary focus of this study (from 6.2879 to 16.1345 m^2/g).
- Regarding photocatalytic performance, after an additional 90 min of visible light exposure, the Bi_2O_3/Kaolin composite exhibited the highest degradation efficiency at 50.9%, compared to pure Bi_2O_3, which achieved approximately 42.0%. For the

recycled Bi_2O_3/Kaolin composite, the degradation efficiency decreased from 50.9% to 32.3% and further declined to 25.5% after three recycling cycles.

Overall, Bi_2O_3 remains the primary photoactive phase, while Kaolin serves as a supporting adsorbent, facilitating the adsorption process prior to photocatalysis.

Author Contributions: Conceptualization, D.C.; data curation, P.T., P.P., S.S. and D.C.; funding acquisition, D.C.; methodology, P.T., P.P. and S.S.; formal analysis, P.T., P.P., S.S., P.J. and D.C.; investigation, P.T., P.P., S.S., P.J. and D.C.; resources: P.J. and D.C.; writing—original draft preparation, P.T., P.J. and D.C.; supervision, D.C.; writing—review and editing, P.T. and D.C. All authors have read and agreed to the published version of the manuscript.

Funding: This research was funded by Naresuan University (NU), and the National Science Research and Innovation Fund (NSRF). Grant No. R2567B013. The authors would like to acknowledge the Tuition Fee Grant for graduate students from the Faculty of Science, Naresuan University.

Institutional Review Board Statement: Not applicable.

Informed Consent Statement: Not applicable.

Data Availability Statement: Data are contained within the article.

Acknowledgments: This work was supported by Naresuan University (NU), and National Science, Research and Innovation Fund (NSRF). Grant No. R2567B013. The authors would like to acknowledge the Tuition Fee Grant for graduate students from the Faculty of Science, Naresuan University. The author also acknowledge the assistance with measurement and data analysis of the EIS Nyquist plot provided by the lab of Tawat Suriwong at the School of Renewable Energy and Smart Grid Technology.

Conflicts of Interest: The authors declare no conflicts of interest.

References

1. Dharma, H.N.C.; Jaafar, J.; Widiastuti, N.; Matsuyama, H.; Rajabsadeh, S.; Othman, M.H.D.; Rahman, M.A.; Jafri, N.N.M.; Suhaimin, N.S.; Nasir, A.M.; et al. A review of titanium dioxide (tio$_2$)–based photocatalyst for oilfield–produced water treatment. *Membranes* **2022**, *12*, 345. [CrossRef] [PubMed]
2. Apopei, P.; Catrinescu, C.; Teodosiu, C.; Royer, S. Mixed–phase TiO_2 photocatalysts: Crystalline phase isolation and reconstruction, characterization and photocatalytic activity in the oxidation of 4–chlorophenol from aqueous effluents. *Appl. Catal. B Environ.* **2014**, *160–161*, 374–382. [CrossRef]
3. Lv, X.; Lam Frank, L.Y.; Hu, X. A Review on bismuth oxyhalide (BiOX, X=Cl, Br, I) based photocatalysts for wastewater remediation. *Front. Catal.* **2022**, *2*, 839072. [CrossRef]
4. Chang, A.M.; Chen, Y.H.; Lai, C.C.; Pu, Y.C. Synergistic effects of surface passivation and charge separation to improve photo–electrochemical performance of BiOI nanoflakes by Au nanoparticle decoration. *ACS Appl. Mater. Inter.* **2021**, *13*, 5721–5730. [CrossRef] [PubMed]
5. Chang, X.; Huang, J.; Cheng, C.; Sui, Q.; Sha, W.; Ji, G.; Deng, S.; Yu, G. BiOX (X = Cl, Br, I) photocatalysts prepared using $NaBiO_3$ as the Bi Source: Characterization and catalytic performance. *Catal. Commun.* **2010**, *11*, 460–464. [CrossRef]
6. Ren, X.; Wu, K.; Qin, Z.; Zhao, X.; Yang, H. The construction of type II heterojunction of Bi_2WO_6/BiOBr Photocatalyst with Improved Photocatalytic Performance. *J. Alloys Compd.* **2019**, *788*, 102–109. [CrossRef]
7. Zhang, L.; Xu, T.; Zhao, X.; Zhu, Y. Controllable synthesis of Bi_2MoO_6 and effect of morphology and variation in local structure on photocatalytic activities. *Appl. Catal. B Environ.* **2010**, *98*, 138–146. [CrossRef]
8. Chen, S.H.; Jiang, Y.S.; Lin, H.Y. Easy Synthesis of $BiVO_4$ for photocatalytic overall water splitting. *ACS Omega.* **2020**, *5*, 8927–8933. [CrossRef]
9. Channei, D.; Thammaacheep, P.; Kerdphon, S.; Jannoey, P.; Khanitchaidecha, W.; Nakaruk, A. Domestic microwave–assisted synthesis of Pd doped–$BiVO_4$ photocatalysts. *Inorg. Chem. Commun.* **2023**, *150*, 110478. [CrossRef]
10. Qiu, T.; Liu, S.; Cai, H.; Zhou, Y.; Chen, K.; Huang, Y.; Feng, Q. One step solid–state reaction synthesis, characterization, and catalytic performance of n–p SnO_2/Bi_2O_3 composite. *J. Mater. Sci. Mater. Electron.* **2018**, *29*, 17463–17472. [CrossRef]
11. Sohail, A.; Shah, M.A.; Majid, K. Ultrathin α–Bi_2O_3 Nanosheets prepared via hydrothermal method for electrochemical supercapacitor applications. *ECS J. Solid. State Sci. Technol.* **2023**, *12*, 011001. [CrossRef]
12. Mallahi, M.; Shokuhfar, A.; Vaezi, M.R.; Esmaeilirad, A.; Mazinani, V. Synthesis and characterization of bismuth oxide nanoparticles via sol–gel method. *Am. J. Eng. Res.* **2014**, *3*, 162–165.
13. Senthamilselvi, R.; Velavan, R. Microstructure and photocatalytic properties of bismuth oxide (Bi_2O_3) nanocrystallites. *Malaya J. Math.* **2020**, *2*, 4870–4874.

14. Azizian–Kalandaragh, Y.; Sedaghatdoust–Bodagh, F.; Habibi–Yangjeh, A. Ultrasound–assisted preparation and characterization of β–Bi_2O_3 nanostructures: Exploring the photocatalytic activity against rhodamine B. *Superlattices Microstruct.* **2015**, *81*, 151–160. [CrossRef]
15. Yahyazadehfar, M.; Sheikhhosseini, E.; Ahmadi, S.A.; Ghazanfari, D. Microwave–assisted synthetic method of novel Bi_2O_3 nanostructure and its application as a high–performance nano–catalyst in preparing benzylidene barbituric acid derivatives. *Front. Chem.* **2022**, *10*, 951229. [CrossRef]
16. Lu, H.; Hao, Q.; Chen, T.; Zhang, L.; Chen, D.; Ma, C.; Yao, W.; Zhu, Y. A high–performance Bi_2O_3/Bi_2SiO_5 p–n heterojunction photocatalyst induced by phase transition of Bi_2O_3. *Appl. Catal. B Environ.* **2018**, *273*, 59–97. [CrossRef]
17. Hou, J.; Yang, C.; Wang, Z.; Zhou, W.; Jiao, S.; Zhu, H. In situ synthesis of α–β phase heterojunction on Bi_2O_3 nanowires with exceptional visible– light photocatalytic performance. *Appl. Catal. B Environ.* **2013**, *142–143*, 504–511. [CrossRef]
18. Elizarraras–Peñaloza, A.; Estrada–Flores, M.; Reza–San Germán, C.M.; Manríquez Ramírez, M.E.; Díaz Barriga-Arceo, L.G.; Santiago-Jacinto, P. Change of phase from α–Bi_2O_3 to β–Bi_2O_3 using the ceramic microwave–assisted approach and its increase of capacitance. *Superficies y Vacío.* **2019**, *32*, 14–21. [CrossRef]
19. Guo, X.; Liang, T.T.; Rager, M.; Cui, X. Low–temperature controlled synthesis of novel bismuth oxide (Bi_2O_3) with microrods and microflowers with great photocatalytic activities. *Mater. Lett.* **2018**, *228*, 427–430. [CrossRef]
20. Rao, S.S.; Saptami, K.; Venkatesan, J.; Rekha, P.D. Microwave–assisted rapid synthesis of silver nanoparticles using fucoidan: Characterization with assessment of biocompatibility and antimicrobial activity. *Int. J. Biol. Macromol.* **2020**, *163*, 745–755. [CrossRef]
21. Sreeju, N.; Rufus, A.; Philip, D. Microwave–assisted rapid synthesis of copper nanoparticles with exceptional stability and their multifaceted applications. *J. Mol. Liq.* **2016**, *221*, 1008–1021. [CrossRef]
22. Papoulis, D.; Panagiotaras, D.; Tsigrou, P.; Christoforidis, K.C.; Petit, C.; Apostolopoulou, A. Halloysite and sepiolite –TiO_2 nanocomposites: Synthesis characterization and photocatalytic activity in three aquatic wastes. *Mater. Sci. Semicond. Process.* **2018**, *85*, 1–8. [CrossRef]
23. Szczepanik, B. Photocatalytic degradation of organic contaminants over clay–TiO_2 nanocomposites: A review. *Appl. Clay Sci.* **2017**, *141*, 227–239. [CrossRef]
24. Kasumba, A.; Buyondo, H.K.; Kirabira, J.B. A comprehensive review on kaolin as pigment for paint and coating: Recent trends of chemical–based paints, their environmental impacts and regulation. *Case Stud. Chem. Environ. Eng.* **2022**, *6*, 100244.
25. Ekosse, G.I.E. Kaolin deposits and occurrences in Africa: Geology, mineralogy and utilization. *Appl. Clay Sci.* **2010**, *50*, 212–236. [CrossRef]
26. Oliveira, W.V.; Morais, A.S.; Honorio, L.M.C.; Trigueiro, P.A.; Almeida, L.C.; Garcia, R.R.P.; Viana, B.C.; Furtini, M.B.; Silva–Filho, E.C.; Osajima, J.A. TiO_2 Immobilized on Fibrous Clay as Strategies to Photocatalytic Activity. *Mater. Res.* **2020**, *23*, 20190463. [CrossRef]
27. Zhang, Y.; Gan, H.; Zhang, G. A novel mixed–phase TiO_2/kaolinite composites and their photocatalytic activity for degradation of organic contaminants. *Chem. Eng. J.* **2011**, *172*, 936–943. [CrossRef]
28. Li, X.; Peng, K.; Chen, H. TiO_2 nanoparticles assembled on kaolinites with different morphologies for efficient photocatalytic performance. *Sci. Rep.* **2018**, *8*, 11663. [CrossRef]
29. Oluwole, A.O.; Olatunji, O.S. Photocatalytic degradation of tetracycline in aqueous systems under visible light irridiation using needle–like SnO_2 nanoparticles anchored on exfoliated g–C_3N_4. *Environ. Sci. Eur.* **2022**, *34*, 5. [CrossRef]
30. Bui, T.S.; Bansal, P.; Lee, B.K.; Mahvelati–Shamsabadi, T.; Soltani, T. Facile fabrication of novel Ba–doped g–C_3N_4 photocatalyst with remarkably enhanced photocatalytic activity towards tetracycline elimination under visible–light irradiation. *Appl. Surf. Sci.* **2020**, *506*, 144184. [CrossRef]
31. Rosario, D. Misuse of Beer–Lambert Law and other calibration curves. *R. Soc. Open Sci.* **2022**, *9*, 211103.
32. Balakrishnan, A.; Gopalram, K.; Appunni, S. Photocatalytic degradation of 2,4–dichlorophenoxyacetic acid by TiO_2 modified catalyst: Kinetics and operating cost analysis. *Environ. Sci. Pollut. Res.* **2021**, *28*, 33331–33343. [CrossRef] [PubMed]
33. Ali, H.; Jana, N.R. Plasmonic photocatalysis: Complete degradation of bisphenol A by a gold nanoparticle–reduced graphene oxide composite under visible light. *Photochem. Photobiol. Sci.* **2018**, *17*, 17628–17637. [CrossRef]
34. Essawy, A.A.; El-Massry, K.F.; Alsohaimi, I.H.; El-Ghorab, A. Managing Encapsulated Oil Extract of Date Seed Waste for High Hydroxyl Radical Scavenging Assayed via Hybrid Photo-Mediated/Spectrofluorimetric Probing. *Molecules* **2023**, *28*, 5160. [CrossRef]
35. Abdullah, A.M.; Garcia-Pinilla, M.Á.; Pillai, S.C.; O'Shea, K. UV and Visible Light-Driven Production of Hydroxyl Radicals by Reduced Forms of N, F, and P Codoped Titanium Dioxide. *Molecules* **2019**, *24*, 2147. [CrossRef] [PubMed]
36. Belachew, N.; Hinsene, H. Preparation of cationic surfactant−modified kaolin for enhanced adsorption of hexavalent chromium from aqueous solution. *Appl. Water. Sci.* **2020**, *10*, 38. [CrossRef]
37. Bish, D.L.; Von Dreele, R.B. Rietveld Refinement of Non−Hydrogen Atomic Positions in Kaolinite. *Clays Miner.* **1989**, *37*, 289–296. [CrossRef]
38. Cheng, H.; Baibiao, H.; Jibao, L.; Zeyan, W.; Bing, X.; Xiaoyan, Q.; Xiaoyang, Z.; Ying, D. Synergistic effect of crystal and electronic structures on the visible–light–driven photocatalytic performances of Bi_2O_3 polymorphs. *Phys. Chem. Chem. Phys.* **2010**, *12*, 15468. [CrossRef]

39. Eberl, J.; Kisch, H. Mineralization of Phenol and 4–Chlorophenol Induced by Visible Light and Assisted by Semiconducting β–Bi_2O_3. *Z. Naturforsch B.* **2010**, *65*, 399–404. [CrossRef]
40. Choudhury, B.; Borah, B.; Choudhury, A. Ce–Nd codoping effect on the structural and optical properties of TiO_2 nanoparticles. *Mater. Sci. Eng. B.* **2013**, *178*, 239–247. [CrossRef]
41. Choudhury, B.; Dey, M.; Choudhury, A. Defect generation, d–d transition, and band gap reduction in Cu–doped TiO_2 nanoparticles. *Int. Nano Lett.* **2013**, *3*, 25. [CrossRef]
42. Buckeridge, J.; Butler, K.T.; Catlow, C.R.A.; Logsdail, A.J.; Scanlon, D.O.; Shevlin, S.A.; Woodley, S.M.; Sokol, A.A.; Walsh, A. Polymorph engineering of TiO2: Demonstrating how absolute reference potentials are determined by local coordination. *Chem. Mat.* **2015**, *27*, 3844–3851. [CrossRef]
43. Peng, H.; Guo, R.T.; Lin, H.; Liu, X.Y. Synthesis of Bi_2O_3/g–C_3N_4 for enhanced photocatalytic CO_2 reduction with a Z–scheme mechanism. *RSC Adv.* **2019**, *9*, 37162–37170. [CrossRef]
44. Thao, L.T.S.; Dang, T.T.T.; Khanitchaidecha, W.; Channei, D.; Nakaruk, A. Photocatalytic Degradation of Organic Dye under UV–A Irradiation Using TiO_2–Vetiver Multifunctional Nano Particles. *Materials* **2017**, *10*, 122. [CrossRef]
45. Poorsajadi, F.; Sayadi, M.H.; Hajiani, M.; Rezaei, M.R. Synthesis of CuO/Bi_2O_3 nanocomposite for efficient and recycling photodegradation of methylene blue dye. *J. Environ. Anal. Chem.* **2020**, *102*, 7165–7178. [CrossRef]
46. Bouziani, A.; Yahya, M.; Bianchi, C.L.; Falletta, E.; Celik, G. Ternary Polyaniline@Bi_2O_3-BiOCl Nanocomposites as Innovative Highly Active Photocatalysts for the Removal of the Dye under Solar Light Irradiation. *Nanomaterials* **2023**, *13*, 713. [CrossRef] [PubMed]
47. Wang, M.; Li, C.; Liu, B.; Qin, W.; Xie, Y. Facile Synthesis of Nano-Flower β-Bi_2O_3/TiO_2 Heterojunction as Photocatalyst for Degradation RhB. *Molecules* **2023**, *28*, 882. [CrossRef] [PubMed]